Edge turbulent transport towards the L-H transition in ASDEX Upgrade and JET-ILW

N. Bonanomi[1], C. Angioni[1], U. Plank[1], P. A. Schneider[1],
C. F. Maggi[2], the ASDEX Upgrade Team[*],
the EUROFusion MST1 Team[**] and JET Contributors[***]

1) Max Planck Institute for Plasma Physics, Boltzmannstr. 2, 85748 Garching, Germany
2) Culham Centre for Fusion Energy, Abingdon, OX14 3DB, UK
*See the author list of H. Meyer et al 2019 Nucl. Fusion 59 112014
**See author list of B. Labit et al. 2019 Nucl. Fusion 59 086020
***See the author list of E. Joffrin et al. 2019 Nucl. Fusion 59 112021

Corresponding author: Nicola Bonanomi, nicola.bonanomi@ipp.mpg.de

Abstract

This work combines experimental observations from the ASDEX Upgrade and the JET-ILW tokamaks and related gyro-kinetic simulations on the L-mode edge turbulence with different isotopes. The evolution of the edge logarithmic gradients and of the edge radial electric field with increasing input power and the correlation between the two are studied. It is found that the edge ion temperature profile plays the dominant role for the evolution of the edge radial electric field in the considered cases. More input power and ion heat flux are needed in hydrogen to obtain values of T_i and R/L_{Ti} similar to the ones observed in deuterium. As a consequence, more power is needed in hydrogen to develop values of the edge radial electric field similar to those in deuterium plasmas. These observations point to a key role of the dependence of the edge turbulence on the main ion mass in determining the different L-H power thresholds with different isotopes. This dependence is found in gyro-kinetic simulations to be connected to the parallel electron dynamics, i.e. to a different kinetic response of passing electrons with different main ion mass. The gyro-kinetic simulations indicate different roles of R/L_{Te} , R/L_{Ti} and R/L_n in driving or stabilizing the edge turbulence at different wave-lengths and indicate a strong role of the external flow shear in stabilizing the edge turbulence. The simulations indicate also that instabilities at finite values of k_x play an important role in edge conditions.

1 Introduction

The plasma edge, that is the region of the confined plasma nearby the last closed flux surface (approximately $0.95 < \rho_{pol} < 1$), plays the dominant role in determining the confinement regime in a tokamak. The low (L-) and high (H-) mode confinement, as well as some ELM-free regimes with high confinement, for example the I-mode [1, 2] and the stationary EDA H-mode [3, 4], are related to the properties of turbulence and transport in this region. The edge turbulent transport also determines the pedestal profile behavior inter-ELM, which affects the way and where the MHD peeling ballooning limit is reached. The impact of a change of the main ion species on the global confinement is also mainly governed by the plasma edge behavior. The accessibility of the H-mode confinement is regularly observed to require about a factor of 2 more power in hydrogen than in deuterium [5, 6]. A strong increase of edge transport is observed in both ASDEX Upgrade and JET-ILW L-modes when moving from deuterium to hydrogen plasmas [7, 8]. The different edge particle transport with different isotopes leads to differences in the gas puff level required in order to obtain similar densities in hydrogen and deuterium L-modes in JET-ILW [7]. In ASDEX Upgrade, when a similar gas puff level is applied in hydrogen and deuterium L-modes, although similar densities can be reached, the edge density logarithmic gradients showed the tendency of being higher in deuterium, as observed in ref. [9]. These differences in the edge particle transport with different isotopes play an important role not only in providing different contributions to the equilibrium radial electric field, potentially affecting the L- to H-mode transition, but also in the H-mode pedestal [10, 11, 12], where it determines the shape of the plasma profile, with a consequent impact on the pedestal stability against peeling and ballooning modes. All of these considerations strongly motivate to undertake the study of the edge turbulence and of its dependence on the main ion mass.

Past studies [13, 14, 15, 16, 17] revealed some of the properties of the L-mode edge turbulence. Local gyro-kinetic simulations, carried out using experiment-relevant plasma parameters as input and that focused on the effect of the isotope mass on the edge turbulence, confirmed most of these properties and were able to reproduce quantitatively the experimental heat fluxes and their trend with the isotope mass[8]. The main instability in the L-mode edge of both ASDEX Upgrade and JET-ILW was found to be an electron drift-wave instability exhibiting a minimum in its linear growth rate as a function of the collisionality ν_e^*. The experimental values of ν_e^* are generally found to be lying around this minimum. This means that in the L-mode edge experimental range of ν_e^*, the dominant instabilities exhibits a resistive nature. Strong non-linear electromagnetic effects were observed in the gyro-kinetic simulations, with an enhancement of the low k_y ($k_y \rho_s \lesssim 0.2$) turbulence and of the turbulent fluxes over a threshold in β_e. This threshold was observed to be consistently lower than the linear threshold of MHD-like instabilities such as KBM (kinetic ballooning modes) [8, 13], found to be linearly stable. The simulations indicated also that at the high edge collisionality both the dominant linear

instability and the turbulence are strongly influenced by the parallel electron dynamics and by the isotope mass [8].

In this paper, starting from what learned in ref. [8], we continue the study on the effect of the isotope mass on the edge turbulence and we analyze the role of the different edge logarithmic gradients and of the external flow shear in driving or stabilizing the edge turbulence. Regarding the role of the isotope mass, we identify the origin of its strong effect in the electron parallel dynamics, i.e. in the L-mode edge the main ion mass strongly influence the kinetic response of the passing electrons. This confirm the results in ref. [8], where a strong role of the passing electron dynamics was related to the high edge collisionality, and is in agreement with what reported in recent publications [18, 19]. Regarding the role of the edge logarithmic gradients, some considerations have to be made first. The ion and the density logarithmic gradients can have a direct effect on the turbulence, as drive of the linear instabilities, but can also have an indirect effect through their impact on the radial electric field and consequently on the external $E \times B$ flow shear, that acts as a stabilization mechanism for the turbulence [20, 21]. This is due to the relation between the radial electric field and the ion diamagnetic term in the radial ion force balance equation. Furthermore, as we show also in this work, the different normalized gradients can behave independently from each other in the plasma edge. Pedestals in T_e are observed at low density with ECRH power only, even if T_i and n_e do not evolve [34], and pedestal formations in T_e and T_i are observed in the I-mode regimes, while n_e remains at L-mode levels [22, 23]. These observations suggest that the different normalized gradients can have different roles in driving or stabilizing the edge turbulence. This is why it is important to study the independent variation of these quantities in the experiment.

For this purpose, we analyze hydrogen and deuterium plasmas in ASDEX Upgrade and JET-ILW with increasing heating power moving from L-mode toward H-mode. We identify the experimental range of variation of the edge logarithmic gradients and of the edge radial electric field E_r, finding an important correlation between the evolution of the ion temperature profile and E_r. Starting from these experimental parameters, scans in the different edge normalized gradients and in the external flow shear are performed in gyro-kinetic simulations to study their isolated effect on the edge turbulence. This leads to two important observations. First, temperature logarithmic gradients drive turbulence at low toroidal wave-numbers while the density logarithmic gradient is a strong drive for the intermediate toroidal wave-numbers turbulence. Second, and related to the previous point, that the concomitant evolution of the ion temperature logarithmic gradient and the radial electric field is more favorable than the concomitant evolution of the density logarithmic gradient and the radial electric field for the suppression of the edge turbulence through the external flow shear. These results go in the right direction to explain the importance, observed in ASDEX Upgrade and Alcator C-Mod experiments [24, 25], of the ion heat flux in determining the L-H power threshold.

Finally, theory based reduced models, as quasi-linear models, for the edge turbulent transport are one of the key elements which are still missing for the prediction of future reactors

plasmas. In this work we compare linear and non-linear results trying to understand the feasibility of the application of quasi-linear models in edge conditions. This comparison gives important indications for the future development of reduced models of the edge turbulence, in particular it indicates the importance of finite k_x instabilities for the nonlinear turbulence.

The paper is organized as follow: in section 2 we report the experimental settings and results in ASDEX Upgrade and JET-ILW, section 3 is dedicated to the gyro-kinetic analysis and in section 4 conclusions are drawn.

2 Experiments in ASDEX Upgrade and JET-ILW

2.1 Experimental settings

The experimental data analyzed in this paper are from the ASDEX Upgrade tokamak (AUG, major radius $R_0 = 1.65\,\mathrm{m}$, minor radius $a = 0.5\,\mathrm{m}$) with a full tungsten wall and from the JET tokamak (major radius $R_0 = 2.96\,\mathrm{m}$, minor radius $a = 1\,\mathrm{m}$) with the ITER-like wall, i.e. with a tungsten divertor and a beryllium main chamber. All the discharges analyzed in this work are in favorable configuration, i.e. with the ion ∇B-drift pointing to the X-point. In AUG the toroidal magnetic field was kept at $B_T = -2.5\,\mathrm{T}$, while two different core line averaged densities were used, $\bar{n}_e \approx 2\,10^{19}\,\mathrm{m}^{-3}$ and $\bar{n}_e \approx 3.5\,10^{19}\,\mathrm{m}^{-3}$, as well as two values of the plasma current, $I_p = 0.8, 1.2\,\mathrm{MA}$, corresponding to $q_{95} = 5, 3.6$ (see Table1). In JET-ILW the core line averaged density was kept around $\bar{n}_e \approx 3.5\,10^{19}\mathrm{m}^{-3}$ while $I_p = 2.5\,\mathrm{MA}$ and $B_T = 3\,\mathrm{T}$ (see Table1). In both devices, the toroidal magnetic field, the plasma current, the plasma shape and the plasma density were kept similar with different isotopes.

Scans in heating power have been performed in hydrogen (H) and deuterium (D) plasmas. The AUG plasmas were mainly heated using electron cyclotron heating (ECRH), with neutral beam injection (NBI) blips of $\Delta t \sim 16\,\mathrm{ms}$ used for the charge exchange (CX) measurements of the ion temperature. Small ECRH steps of around $200 - 300\,\mathrm{kW}$ were applied for the power scan, with each step lasting $200 - 400\,\mathrm{ms}$. The JET-ILW plasmas were heated using NBI heating, with power steps of $\sim 1.2\,\mathrm{MW}$. The quantity P_{net}/P_{L-H}, where P_{net} is the sum of the heating powers (NBI+ECRH+ohmic power) minus the time derivative of the plasma stored energy ($P_{net} = P_{ECRH} + P_{NBI} + P_{ohm} - \dot{W}_{MHD}$) and P_{L-H} is the same quantity calculated at the L-H transition for each plasma (just before the improvement in confinement), is used in this paper for the comparison of the evolution of the edge profiles in different isotopes and in different devices. It is worth noticing that in hydrogen the quantity P_{L-H} is usually twice than in deuterium. In order to simplify the comparison with other studies on the L-H transition, the radiated power P_{rad} was not taken into account in the calculation of P_{net}, as it was done in these past studies [26, 27] . Furthermore, as also observed for the AUG cases in ref. [26], no systematic dependence of P_{rad} on the applied external heating or on the plasma composition was found.

For both devices a feedback control of the line averaged density was used to keep the density profiles as constant as possible and as similar as possible between hydrogen and deuterium. It is observed in both AUG and JET-ILW that more gas puff is needed in hydrogen to obtain similar densities as in deuterium [7, 9]. For this scope, in some of the studied cases, up to the double of the gas puff level used in the corresponding deuterium cases was necessary in hydrogen in order to have a similar density.

The electron temperature (T_e) profiles in both devices were measured using the ECE (Electron Cyclotron Emission) and the core and edge Thomson scattering diagnostics (the high resolution Thomson scattering (HRTS) signal in JET-ILW). The ion temperature (T_i) profiles in both devices were measured using the core and edge CX diagnostics. It must be noticed that for the $I_p = 0.8$ MA cases in AUG the CX signals were low and the measurements of T_i have larger errors than at $I_p = 1.2$ MA. The electron density profiles (n_e) were obtained using the HRTS and the reflectometer signals for JET-ILW and using the Thomson scattering, the interferometers signals and the fits performed using the integrated data analysis (IDA) Bayesian approach [28] in AUG. For the alignment of the edge profiles the signals of T_e were moved in order to have $70 \lesssim T_e \lesssim 100$ eV at the separatrix in L-mode. The corresponding signals of the electron density (Thomson scattering signals) were moved accordingly. These values of the electron temperature at the separatrix are deduced from considerations on the heat transport in the scape-off-layer (SOL), using the Spitzer-Haerm heat conductivity model (this is implemented in the IDA routines), and from EDGE2D/EIRENE simulations for the JET cases[7]. Regarding T_i, as no simple assumptions can be made on the ion temperature at the separatrix, we simply checked that the values of T_i/T_e at the separatrix would not exceed $\approx 1.5 - 2$. The error introduced by moving the T_i measurements of ± 7 mm, that is the CX radial error, is taken into account in the error bars of R/L_{Ti}. A new diagnostic, based on the active spectroscopy of helium II lines and capable of measuring the radial electric field (E_r) around the separatrix [29], has been used for the study of the evolution of the edge E_r in AUG. The values of the normalized gradients R/L_{Te}, R/L_{Ti} and R/L_n reported in this work are calculated using the plasma major radius (R_0) as normalization length and the plasma minor radius, r, for the calculations of the gradients (for example: $R/L_{Te} = -R_0 \nabla_r T_e/T_e$). All the quantities related to the plasma equilibrium (radii, q profiles etc.) and used in this work have been reconstructed using the EFIT routines [30, 31] for JET and with the CLISTE routines [32] for AUG.

More details on the JET-ILW discharges can be found in ref. [7], while more details on some of the studied AUG discharges are reported in ref. [9, 26]. In table 1 the list of the analyzed discharges as well as their main plasma parameters are given. An example of the evolution of the plasma profile with increasing heating power is shown in figure1 for AUG discharge #37909 in deuterium. Our study is carried out mainly at the toroidal radius $\rho_{tor} = 0.95$, where $\rho_{tor} = \sqrt{\Phi/\Phi_{max}}$, Φ being the toroidal magnetic flux and Φ_{max} its value at the separatrix. This radial position corresponds to $\rho_{pol} \approx 0.98$.

2.2 Experimental observations

The values of R/L_{Te}, R/L_{Ti} and R/L_n calculated at $\rho_{tor} = 0.95$ from the ASDEX Upgrade and the JET-ILW plasmas are shown in figure 2 as a function of P_{net}/P_{L-H}. We remind that P_{L-H} in hydrogen is roughly the double than in deuterium. For the AUG cases the full colored marks represent plasmas at $I_p = 1.2$ MA, while the matte color (dark grey for D and violet for H) crosses and X represent plasmas at $I_p = 0.8$ MA. In general the values of the edge normalized gradients are found to be very similar in AUG and JET-ILW (figure 2b).

R/L_n does not exhibit a strong variation with increasing input power, not even after the L-H transition where an evolution of the edge density is visible in the experiment. It is important to remind that in these discharges a feedback control of the line averaged density was used and this might contribute to the low evolution of the L-mode edge density. For both devices, more gas puff was needed in hydrogen in order to obtain densities similar to those in deuterium plasmas. In JET-ILW ~30% more gas puff was used and, despite this, slightly higher values of R/L_n are observed in deuterium. In AUG 0-30% more gas puff was used, at the same level of heating power, in hydrogen. Similar values of R/L_n between hydrogen and deuterium are observed in our AUG cases but, when the same gas puff level is applied at similar values of P_{net}/P_{L-H}, higher values of R/L_n are generally observed in deuterium as reported in [9].

For both devices R/L_{Te} and R/L_{Ti} are observed to evolve with increasing heating power, reaching values at $P_{net}/P_{L-H} = 1$ larger than those at $P_{net}/P_{L-H} < 1$, and continue to increase after the L-H transition. In the AUG ECRH heated plasma at low density ($\bar{n}_e \sim 2\,10^{19}\mathrm{m}^{-3}$), R/L_{Te} evolves more than R/L_{Ti} while, at $\bar{n}_e \sim 3\,10^{19}\mathrm{m}^{-3}$, R/L_{Ti} exhibits a stronger variation comparable to that of R/L_{Te}. This behavior can be related to the fact that, with ECRH only and at low density, the heating power is predominantly directed to electrons with low exchanged power between electrons and ions. In this situation a pedestal can form in T_e when increasing the input power, while T_i and R/L_{Ti} remain almost constant. This behavior has been observed also in past studies [34]. More input power is needed in hydrogen to obtain values of R/L_{Ti} similar to the deuterium ones, although hydrogen has higher levels of the ion heat flux due to stronger thermal coupling than deuterium (figure 9).

The evolution of the minimum of the edge radial electric field E_r in the AUG plasmas with $I_p = 1.2$ MA is shown in figure 3. In figure 3a as a function of P_{net}/P_{L-H} and in figure 3b as a function of the ion diamagnetic term in the ion radial force balance equation, $-T_i/(q_i R_0)\,(R/L_{Ti} + R/L_n)$, measured at $\rho_{tor} = 0.95$. This radial position corresponds roughly to the position where the minimum values of E_r are generally located. In deuterium plasmas, the minimum of E_r strongly evolves with increasing input power and a clear correlation with the ion diamagnetic term is observed. In hydrogen plasmas, the E_r minima behave similarly than in deuterium, but higher values of the input power are needed to obtain the same values. Considering the behavior of R/L_n in these plasmas, it is clear that the edge ion temperature profile, through $T_i\,(R/L_{Ti})$, and its response to an increase of the heating power determine the

evolution of the edge radial electric field. This confirms what found in ref. [24, 25, 27, 35, 36], i.e. that the edge ion heat flux and the evolution of the edge ion temperature are key elements for the evolution of the edge radial electric field and for the L-H transition. The higher edge turbulence with lower isotope mass [8, 18] can then be the responsible for the lower evolution of R/L_{Ti} and of E_r with increasing heating power and for the higher L-H power threshold in hydrogen.

Finally, the experimental values of the electron and ion heat transport coefficients, $\chi_{e,i}(\mathrm{m}^2/\mathrm{s})$ averaged on $0.92 < \rho_{tor} < 0.98$, for the AUG discharges at $I_p = 1.2\,\mathrm{MA}$ are shown in figure 9 as a function of the electron and ion heat fluxes measured at $\rho_{tor} = 0.95$. Similar values are observed in the discharges with $I_p = 0.8\,\mathrm{MA}$. These experimental fluxes and transport coefficients are evaluated using ASTRA [37, 38] power balance calculations. Blue triangles indicate D discharges while black triangles indicate H plasmas. The ion heat fluxes at the L-H transition are higher in hydrogen, that features also higher transport coefficients, indicating again the role of turbulent transport in the isotope effect at the edge. For both isotopes, no strong evolution of the transport coefficients with input power is visible. In fact they stay at the same level also towards the L-H transition. This indicates that the turbulence level does not change significantly moving towards the L-H transition. This observation can be related to the increasing effect of the external $E \times B$ flow shear on the turbulence, as indicated in the next section and visible also from the GENE results shown in figure 9.

3 Gyro-kinetic simulation

3.1 Gyro-kinetic simulations set up

Linear and non-linear gyro-kinetic simulations with the GENE (Gyro-kinetic Electromagnetic Numerical Experiment) code [39, 40] have been performed in order to study the micro-instabilities in the plasma edge. GENE solves the gyro-kinetic Vlasov equations [41, 42] coupled with the Maxwell equations within a δf approximation and using a set of field aligned coordinates $\{x, y, z, v_\parallel, \mu\}$. z is the coordinate along the magnetic field line, x is the radial coordinate, y is the binormal coordinate, $v_\parallel$ is the parallel velocity and μ is the magnetic momentum. The simulations are carried out using realistic geometry (reconstructed from numerical equilibrium files provided by equilibrium solvers), collisions (using a Landau-Boltzmann collisional operator), finite β effects (considering both $B_\perp$ and $B_\parallel$ fluctuations) and kinetic ions and electrons using the physical mass ratio. No impurities have been considered in the simulations, the experimental values of Z_{eff} of the discharges being low ($Z_{eff} \approx 1.2$-1.3) as is typical for metal machines, and in order to reduce the simulations CPU-time demand.

The effect of the external flow shear $\gamma_{E \times B}$ has been considered in the simulations. Its values have been calculated using the values of the radial electric field derived using the radial force balance equation for ions starting from the experimental ion pressure profiles and using the

normalized quantity $\hat{\gamma}_{E \times B} = \frac{\rho_{tor}}{q} \frac{d}{d\rho_{tor}} \left(\frac{E_r}{B_{tor}} \right) \frac{\rho_a}{c_s}$, where q is the safety factor, B_{tor} is the toroidal magnetic field and $\rho_a = \sqrt{\Phi_{max}/(\pi B_{tor})} \, (m)$, with Φ_{max} the toroidal flux measured at the last closed flux surface, i.e. at $r/a = 1$. The variation of the normalized external flow shear $\hat{\gamma}_{ExB}$ with R/L_{Ti} and R/L_n is calculated simply using the different values of R/L_{Ti} and R/L_n in the ion diamagnetic term of the radial force balance equation for determining the profile of the edge radial electric field: $E_r \approx -\frac{T_i}{R_0 q_i}(\frac{R}{L_{Ti}} + \frac{R}{L_{n_i}})$. However, as the external flow shear is a derivative of the E_r, modification in E_r by the other terms in the ion radial force balance equation, i.e. the plasma velocities, can determine changes in $\gamma_{E \times B}$. Furthermore, changes in T_i can also affect E_r and $\gamma_{E \times B}$. It must also be noticed that the neoclassical poloidal velocity is also proportional to R/L_{Ti} [45], as also is the difference between the impurity and main ion toroidal velocity [45]. All these aspects imply some approximations and limitations and introduce uncertainties when calculating $\hat{\gamma}_{E \times B}$ considering only the ion diamagnetic term as we did for this work.

Typical grid parameters in the non-linear simulations were as follows: perpendicular box sizes $[L_x, L_y] \approx [200, 250]\rho_s$, phase-space grid discretization $[n_x, n_y, n_z, n_{v\parallel}, n_\mu] \approx [384, 96, 72, 48, 16]$ using $0.025 \lesssim k_y \rho_s \lesssim 1.9$ and $0.025 \lesssim k_x \rho_s \lesssim 7$. Lower values of k_y, k_x, using $0.013 \lesssim k_y \rho_s \lesssim 1.2$ and $0.016 \lesssim k_x \rho_s \lesssim 8$ have also been used for convergency tests. All the simulations in this work have been done in the local flux-tube limit. This choice has been dictated by the fact that the present global electromagnetic version of the code is unstable when the magnetic field fluctuations play an important role (as it is in present cases). This is not always observed but it is the case in many edge conditions and it is related to numerical instabilities present in the code and not to physical reasons. A new version of the global GENE solver, stable even in the electromagnetic cases, should be available soon. Considering the values of the gradients lengths typical of the edge region that has been considered in our cases, we have values of $\rho_s/L_\perp (\approx \rho_s/L_{Te,i} \text{ or } \rho_s/L_n) \approx 1/200 - 1/80$. Considering the results obtained in ref.[43, 44] (based on the Cyclone Base case, adiabatic electrons and in the electrostatic approximation), for our cases, global effects could play a quantitative role in edge conditions reducing the predicted fluxes, especially when approaching the H-mode pedestal conditions. Nevertheless, the good agreement between the local simulation and the experimental observations obtained in ref. [8], where dedicated convergence tests were made, and in this work support the reliability of the results obtained with local simulations in L-mode edge conditions.

The gyro-kinetic simulations reported here are performed using the experimental parameters of AUG hydrogen shot #35229 at $t = 1.8 \, s$ (with ECRH power just below the H-mode power threshold) and at $\rho_{tor} = 0.95$. Starting from their experimental range reported in section 2, scans in the values of $R/L_{Ti}, R/L_{Te}, R/L_n$ and $\gamma_{E \times B}$ have been performed in the simulations while keeping all the other parameters constant. Linear simulations were performed also for JET-ILW founding, as in ref.[8], similar results as for AUG. For this reason, and for a direct comparison between linear and non-linear results, we show only simulations performed for the AUG cases.

3.2 Role of the parallel electron dynamic in the isotope effect

As observed in ref. [8], the edge high collisionality determines the passing electron dynamics to be fundamental for the L-mode edge turbulence. In these conditions also the effect of the isotope mass was found to be important. Wider parallel structure of the electrostatic potential were observed with lower isotope mass [8], indicating a dominant role of the passing electron dynamics. The term related to the parallel electron dynamics in the gyro-kinetic equations is written, in GENE units [40], as:

$$C_m \left\{ -\hat{v}_{e,th} \frac{\hat{C}}{JB_0} \left[v_\parallel \left(\frac{\partial f_{e,1}}{\partial z} - \frac{e}{T_e} F_{e,o} \frac{\partial \phi}{\partial z} + F_{e,0} \mu \frac{\partial B_{1,\parallel}}{\partial z} \right) - \mu \frac{\partial}{\partial z} \left(B_o \frac{\partial f_{e,1}}{\partial v_\parallel} \right) \right] \right\} \tag{1}$$

where the ratio between the electron and the ion mass, m_e/m_i, enters towards $\hat{v}_{e,th} = \sqrt{T_e/(m_e/m_i)}$, m_i being used as reference mass in our simulations. $\hat{C}, J, B_0$ are factors related to the plasma geometry and the background magnetic field, F_0, f_1 are the background (Maxwellian) and the perturbed parts of the electron distribution function and $\phi, B_{1,\parallel}$ represent the perturbed electrostatic potential and the parallel fluctuations of the magnetic field. C_m is a coefficient inserted in order to test the effect of changing the mass ratio m_e/m_i in this term while keeping its physical value in the rest of the equations. By artificially changing the value of C_m, it is then possible to have hydrogen values of $\hat{v}_{th,e}$ in the parallel electron dynamics term in deuterium simulations and vice versa (setting $C_m = 1.4$ in D simulations and $C_m = 0.7$ in H simulations).

In figure 4 the linear growth rate of the main instability from AUG linear simulations are shown as a function of the collisionality ν_e^*. The simulations are done using $k_y \rho_s = 0.2$, where the non-linear fluxes usually peak in the non-linear electrostatic simulations, but similar results are obtained using different values of k_y in the range important for the nonlinear fluxes. As observed in [8], the linear growth rates are higher in hydrogen, especially around the minimum in growth rate but, by artificially changing C_m, the linear growth rates of deuterium simulations are recovered in hydrogen simulations and vice versa. This demonstrates that the electron parallel dynamics in eq. 1 determines the variation of the growth rates with different isotopes. This result, obtained in a range of parameters relevant for L-mode edge conditions at ASDEX Upgrade and JET-ILW, indicates that the different kinetic response of the electrons with different main ion mass is the responsible for the strong deviation from the gyro-Bohm expectations observed experimentally an in the simulations. These results also imply that, in the general conditions when the turbulence is determined by the parallel electron dynamics, i.e. when the electron response is very far from being adiabatic, the corresponding term in the gyro-kinetic equation, that depends on m_e/m_i, can give a strong deviation from gyro-Bohm expectations.

These results are in complete agreement with what has been recently found in ref. [18, 19] and confirm the importance of this physics mechanism for the reversal of the gyro-Bohm scaling in the experimental conditions of AUG and JET-ILW edge plasmas. It is also worth noticing that other terms in the gyro-kinetic equation depend on m_e/m_i, i.e. those related to finite

Larmor-radius effects (gyro-averaging of the potentials fluctuations). These terms have been also analyzed founding that they have a negligible contribution to the effect of m_e/m_i on the linear growth rates, at least in the considered range of k_y.

3.3   Effects of the normalized gradients on the edge turbulence

In the following we report the results from linear and non-linear simulations performed scanning $R/L_{Ti}, R/L_{Te}, R/L_n$ and $\gamma_{E \times B}$ while keeping the other parameters unchanged. The values of $R/L_{Ti}, R/L_{Te}, R/L_n$ considered for these scans are taken in the experimental range of values reported in section 2 and are: $R/L_{Ti} = (21, 42, 63), R/L_{Te} = (34, 56, 74), R/L_n = (9, 33, 56)$ and $\hat{\gamma}_{ExB} = (0.2, 0.26, 0.3)$. $\hat{\gamma}_{ExB} = 0.2$ corresponds to the $R/L_{Ti}, R/L_n = 21, 36$ case; $\hat{\gamma}_{ExB} = 0.26$ corresponds to the $R/L_{Ti}, R/L_n = 42, 33$ and to the $R/L_{Ti}, R/L_n = 21, 56$ cases; $\hat{\gamma}_{ExB} = 0.3$ corresponds to the $R/L_{Ti}, R/L_n = 63, 33$ case. When not specified, the nominal experimental values of the normalized gradients of AUG shot #35229 at $t = 1.8$ s are used: $(R/L_{Ti},\ R/L_{Te},\ R/L_n) = (21, 56, 33)$. As nonlinear electromagnetic effects strongly enhance low k_y ($k_y \rho_s \lesssim 0.2$) turbulence in the edge [8, 13], we performed both electrostatic and electromagnetic simulations to differentiate the effect of the normalized gradients in the two cases. Values of the ion heat transport coefficient $\chi_i (m^2/s)$ are mainly shown in the following, since similar behaviors are observed for the electron heat transport and for the particle transport coefficients (respectively χ_e and D). Typical values of $\chi_e (m^2/2)$ and $D(m^2/2)$ are shown in figure 7 and in figure 9.

Effect of R/L_{Ti}

As visible in figure 5a, in linear simulations no strong effect of R/L_{Ti} is observed on the growth rate of low k_y ($k_y \rho_s \lesssim 0.2$) instabilities while R/L_{Ti} is found to stabilize intermediate k_y ($0.2 < k_y \rho_s \leq 1.0$) instabilities. In figure 5d the linear and the main non-linear frequencies, $\omega(\rho_a/c_s)$, are shown. These are generally found to have the electron diamagnetic velocity sign (negative in GENE). The effect of R/L_{Ti} on $\omega(\rho_a/c_s)$ is not strong except at intermediate k_y in the nonlinear electromagnetic case at the higher value of R/L_{Ti}. The typical phase velocity of the turbulence, calculated as $v_{ph} = \omega/k_y$ (m/s) for the electrostatic case $(R/L_{Te}, R/L_{Ti}, R/L_n) = (56, 42, 33)$, is also reported in figure 5g.

The impact of R/L_{Ti} is found to be weak in non-linear electrostatic simulations, with no significant increment of the transport coefficients with increasing R/L_{Ti} (figure 6a). The fluctuations of the electrostatic potential ϕ slightly increase at low k_y when increasing R/L_{Ti} (figure 6c) and the intensity of the cross-phases between ϕ and the perturbed perpendicular electron temperature, $T_{e,\perp}$, increase at low k_y and intermediate k_y, with the cross-phase angles going to values closer to $\pi/2$ (figure 6d). However, the overall effect is weak and the transport coefficients are not strongly affected. When considering $\gamma_{E \times B}$ in the simulations, the level of the turbulence is reduced, but also in this case, when considering its variation in combination

with the variation of R/L_{Ti}, the values of the transport coefficients do not vary substantially.

When considering electromagnetic effects in non-linear simulations, as already observed in the past [8, 13], a strong destabilization of low k_y turbulence ($k_y\rho_s \lesssim 0.3$) is present. In this case R/L_{Ti} is found to be a strong drive for the low k_y turbulence: both the electrostatic potential fluctuations (figure 6c), the $\phi - T_{e,\perp}$ and the $\phi - T_{i,\perp}$ cross-phase intensity increase at $k_y\rho_s \lesssim 0.2$ (figures 6e and 6f), with a substantial enhancement of the transport coefficients with increasing R/L_{Ti} (figure 6b). Nevertheless, $\gamma_{E\times B}$ has a strong impact on this low k_y turbulence and, when its effect is considered, the turbulent heat fluxes and the transport coefficients are strongly reduced and go to experimental levels (figures 6b and 9). Furthermore, when increasing both $\gamma_{E\times B}$ and R/L_{Ti} simultaneously, the transport coefficients in the simulations do not increase with increasing R/L_{Ti}, as observed in the AUG experiments.

Effect of R/L_{Te}

The effect of R/L_{Te} in linear simulations is a destabilization of the main micro-instability at all the considered values of k_y (figure 5b). When increasing R/L_{Te} in nonlinear electrostatic simulations, the electrostatic potential fluctuations slightly increase in the region $0.1 \lesssim k_y\rho_s \lesssim 0.2$ (figure 7c) and the amplitude of the cross-phase between ϕ and $T_{e,\perp}$ peaks in the same region (figure 7d), meaning that R/L_{Te} is enhancing the low k_y turbulence related to the low k_y electron drift-wave instability (for which R/L_{Te} is the main linear drive). Similar effects on the cross-phases between ϕ and n_e and between ϕ and T_i fluctuations are observed, but their values are close to zero in these cases. However, the overall effect of increasing R/L_{Te} is a reduction of the transport coefficients (figure 7a). This is related to the fact that the enhancement of the low k_y fluctuations of ϕ is not strong while, at the same time, there is a shift of the $\phi - T_{e,\perp}$ cross-phases towards lower values (figure 7c). This is related to the drift-wave nature of the turbulence driven by R/L_{Te}. The effect of R/L_{Te} on the turbulence is found to be small also in non-linear electromagnetic simulations, with no significant enhancement of the transport coefficients (figure 7b) nor of the electrostatic potential fluctuations (figure 7c). The overall effect of increasing R/L_{Te} in the simulations is then an increase of the electron heat fluxes but not an enhancement of the transport coefficients.

Effect of R/L_n

Linearly, R/L_n has different effects at different values of k_y: its effect is non-monotonic on low k_y instabilities while it stabilizes intermediate k_y instabilities (figure 5c). Non-linearly, R/L_n is found to be a strong drive for intermediate k_y electrostatic turbulence. When increasing R/L_n in the electrostatic simulations, the electrostatic potential fluctuations and the amplitude of the cross-phases between ϕ and $T_{e,\perp}$ (the same is valid for the cross-phases between ϕ and n_e and between ϕ and T_i fluctuations) are strongly enhanced in the intermediate k_y region (figures 8c and 8b). This results in a strong enhancement of all the transport coefficients (figure 8a).

In the electromagnetic cases, no strong influence of R/L_n on the low k_y turbulence destabilized by electromagnetic effects is observed, but R/L_n still destabilizes intermediate k_y turbulence (figure 8b).

Differently from what found for R/L_{Ti}, $\gamma_{E \times B}$ has a lower impact in these cases, also when considering the simultaneous variation of $\gamma_{E \times B}$ with R/L_n. This can be related to the fact that the intermediate k_y turbulence driven by R/L_n is not strongly affected by $\gamma_{E \times B}$.

3.4   Considerations on the gyro-kinetic simulations

Quasi-linear models for edge turbulence

When low k_y ($k_y \rho_s \lesssim 0.2$) electrostatic turbulence related to electron drift-waves dominates, there is a good agreement between linear and non-linear predictions. Instead, when the nature of the turbulence is more ballooning-like, as for the intermediate k_y turbulence, or when strong electromagnetic effects play a role, the differences between linear and non-linear predictions can become significantly large. This can be seen for example in the comparison of the characteristic frequencies in figure 5: linear and non-linear frequencies compare well in the low k_y region, but can deviate at intermediate k_y. Also looking at the cross-phases angles in figures 6, 7 and 8 it is evident that the linear predictions can be very different from the non-linear results. Furthermore, as described in ref. [8, 14] and observed in the previous section, strong non-linear electromagnetic effects play a role for low k_y spectra of the turbulence.

In the plasma edge conditions studied in this work, it might be also important to look at instabilities centered at finite $k_{x,0}$. In figure 10 the spectra of the electron heat flux at different values of R/L_n as well as the $|\phi|^2 (k_x \rho_s, k_y \rho_s)$ and $|\phi|^2 (k_x \rho_s, z)$ spectra are reported. As visible from figures 10a, 10b, 10c and 10d, finite k_x values are important for the electrostatic potential fluctuations and for the final electron heat fluxes. This is true for all the values of R/L_n considered, the peak of the q_e spectra being located around $k_x \rho_s \approx 0.035$ for all the cases. In figure 11a the linear growth rates of instabilities at $k_y \rho_s = 0.2, 0.4, 0.6$ and centered in the range $-0.4 < k_{x0} < 0.4$ are reported. In figure 11b and 11c the quasi-linear electron heat flux calculated from the same simulations are shown. These are calculated as

$$q_e^{QL} = \sum_{k_y} \frac{\gamma_{k_y}}{\langle k_\perp^2 \rangle} \frac{q_e^{k_y}}{|\phi_{k_y}|^2}$$

where $\langle k_\perp^2 \rangle = \int (g_{yy} k_y^2 + 2 g_{xy} k_x k_y + g_{xx} k_x^2) |\phi|^2 J dk_x dz / \int |\phi|^2 J dk_x dz$, q_e being the linear heat flux at each k_y, J, g_{ij} being geometrical factors. As visible from the plots, the linear growth rates and the quasi-linear fluxes do not always peak at $k_x = 0$, as generally observed for core-like parameters, but finite k_x instabilities can have higher growth rates and higher quasi-linear fluxes. This is clearly visible for the $R/L_n = 56$ case, where the deviation from the results that would be obtained considering only instabilities centered at $k_{x,0} = 0$ are higher. Looking at linear instabilities centered at $k_{x,0} \neq 0$ it is also possible to recover the properties of the nonlinear

turbulence. As an example, for the case $R/L_n = 56$ and $k_y \rho_s = 0.4$ (figure 12), the instability centered at $k_{x,0} = -0.075$, where the growth rate peaks, has a characteristic frequency similar to the nonlinear one (while the instability centered at $k_{x,0} = 0$ has a positive frequency), has parallel structures of the electrostatic potential more ballooned than the instability centered at $k_{x,0} = 0$ and has components of the $\phi - T_{e,\perp}$ cross-phases angle that lay in the same range of the nonlinear ones. These observations indicate that taking into account linear instabilities centered at $k_x \neq 0$ could be important for future attempts of developing reduced models for the edge turbulence. This is not the first time that linear instabilities at finite k_x are studied or observed to be important (see for example ref. [46, 47, 48, 49, 50, 51, 52]).

Missing elements and future steps

In this work we have focused on the isolated effects of the different edge normalized gradients on the edge turbulence. Experimentally many parameters are changing at the same time while approaching the L-H transition. Especially $\nu_e^*, \beta_e, T_e/T_i$ and the geometry could play important roles. The next step will be to study the effects of the variation of all the experimental parameters consistently. This represents a limit of our work, nevertheless our study gives precious information on the isolated effects of the various normalized gradients on the turbulence and this information will be very helpful for the understanding of the results from simulations in which more parameters are changing simultaneously. We report here, as an example, the results from a linear scan made using input parameters taken from AUG shots #36982 in deuterium (see table 1) at different levels of ECRH power. The scan was made using $k_y \rho_s = 0.2$ and scanning in collisionality to see where the minimum in the linear growth rate $\gamma(\nu_e^*)$ is located with respect to the experimental values of ν_e^*. As visible in the plot of figure 13, the experimental points always stay close to the minimum in the growth rate and, despite the increase of R/L_{Te} with increasing ECRH power, the linear growth rates are lower close to the L-H transition ($P_{ECRH} = 2.8\,MW$). In this case this is found to be mostly determined by the change in T_e/T_i. Another aspect is that the values of E_r measured directly in the experiments should be used in the simulations. Unfortunately these values were not available when the simulations were performed but will be used in future simulations. The next step for the validation of our results will be also to test our local simulations against at least one global simulation.

4 Discussion and conclusions

The analysis of the edge turbulent transport and of its dependence on the main ion mass that was started in ref.[8] has been continued in this work. We focus our analysis on three aspects related to the L-mode edge turbulence: its response to the variation of the edge normalized gradients with increasing input power, the effect of the external flow shear and the identification of the physical mechanisms that determine the strong dependence of the edge turbulent transport

13

on the main ion mass. For these purposes, experimental observations from the ASDEX Upgrade and from the JET-ILW tokamaks are combined with related gyro-kinetic linear and non-linear local simulations with the code GENE. For both devices, plasmas with scans in input heating power (mainly ECRH for AUG and NBI for JET-ILW) going from L- to H-mode have been analyzed in hydrogen and in deuterium. This experimental analysis allows us to identify the experimental range of variation of the edge normalized gradients and of the edge radial electric field. These parameters play a critical role for the turbulence as the edge logarithmic gradients represent the main drive for the linear instabilities while the radial electric field determines the external $E \times B$ flow shear that can act as a stabilization mechanism of the turbulence. Furthermore, a relation between the kinetic profiles and the radial electric field exists and is determined by the radial force balance.

In these experiments R/L_n exhibits a limited variation with input heating power, particularly at AUG and in JET-ILW in hydrogen. This is true also in the H-mode phase, where the densities and their gradients are observed to evolve. However, it must be noticed that these discharges have been run with feedback control of the line averaged density and this might have contributed to the limited evolution of R/L_n. In more general operation conditions, as for instance with constant gas puff levels, a change in the L-mode density profile shape can be observed [9]. Differences are also observed in H-mode plasmas [10, 11, 12] and an impact of the density profile on the L-H transition power has been observed as a consequence of the change from carbon to tungsten wall in ASDEX Upgrade [33], although no analysis on the values of the normalized gradients was made in these past studies. For both devices, more gas puff was needed in hydrogen in order to obtain densities similar to the deuterium plasmas ones. In JET-ILW ~30% more gas puff was used in hydrogen and, despite this, slightly higher values of R/L_n are observed in deuterium. Similar values of R/L_n between hydrogen and deuterium are observed in our AUG cases despite the higher gas puff in hydrogen plasmas. Instead, when the same gas puff level is applied at similar values of P_{net}/P_{L-H}, higher values of R/L_n are generally observed in deuterium as reported in [9].

For both AUG and JET-ILW, R/L_{Ti} and R/L_{Te} are observed to evolve with the heating power. While similar values of R/L_{Te} can be obtained in hydrogen and deuterium at similar levels of input power, in both devices much more input power is needed in hydrogen to obtain values of R/L_{Ti} similar to those in deuterium. The edge radial electric field E_r is found, in the AUG cases, to be determined by the ion diamagnetic term in the ion radial force balance equation, i.e. $E_r \approx T_i/(q_i R_0) \, (R/L_{Ti} + R/L_n)$. As in the studied cases it strongly depends on $T_i \, R/L_{Ti}$ (because R/L_n does not vary), it requires more input power in hydrogen to reach values similar to the deuterium ones. This leads also to lower values of the external $E \times B$ flow shear in hydrogen at the same level of input power. These observations point to a dominant role of the turbulent ion heat transport and of its dependence on the main ion mass in determining the different evolution of the edge radial electric field and consequently in determining the differences in the L-H power threshold in different isotopes, at least in the considered cases.

Finally, the experimental values of the edge heat transport coefficients (available only for the AUG cases) are found to be higher in hydrogen than in deuterium, at the same level of the electron and ion heat fluxes. Also the ion heat fluxes at the L-H transition are higher in hydrogen, indicating again the role of turbulent transport in the isotope effect at the edge. Furthermore, for both isotopes, no strong evolution of the transport coefficients with input power is visible. In fact they stay at the same level also towards the L-H transition. This indicates that the turbulence level does not change significantly moving towards the L-H transition. This observation can be related to the increasing effect of the external $E \times B$ flow shear on the turbulence, as indicated by the GENE simulations. Limiting more the evolution of R/L_{Ti} with increasing ion heat flux in hydrogen with respect to deuterium, turbulence limits more also the evolution of the radial electric field in hydrogen and more power is required in hydrogen to reach the L-H transition. Again, we remind that this result was obtained controlling the plasma density and that the role of the particle transport can also be important in other conditions.

The gyro-kinetic analysis confirms what found in previous studies [8, 13], showing that the high edge collisionality, together with the high values of R/L_{Te} and R/L_n, imply that the parallel electron dynamics plays the dominant role for the edge turbulence. For this reason, it is shown in this paper that the different kinetic response of the passing electrons is responsible for the strong effect of the main ion mass on the edge turbulence. This result, obtained using experimental plasma parameters from AUG and JET-ILW L-modes approaching the L-H transition, shows that the impact of the ion mass on the kinetic response of passing electrons determines the reversal of the gyro-Bohm scaling of transport, as regularly observed in edge turbulence. These results confirm recent theoretical studies [18, 19].

The simulations demonstrate different effects of the different normalized gradients on the edge turbulence. R/L_{Te} drives the low k_y ($0.1 \lesssim k_y\rho_s \lesssim 0.3$) electrostatic electron drift-wave turbulence but its effect on the transport coefficients is almost negligible. This is related to a low impact of increasing R/L_{Te} on the electrostatic potential fluctuations amplitude and to a reduction of the $\phi - \widetilde{T}_e$ cross-phase angles. R/L_n strongly drives intermediate k_y ($0.3 \lesssim k_y\rho_s \lesssim 1.0$) turbulence, with more ballooning-like properties, determining a strong enhancement of the transport coefficients. This intermediate k_y turbulence is found to be weakly affected by the external flow shear and increasing $\gamma_{E \times B}$ with increasing R/L_n (through its effect on E_r) does not result in a reduction of the transport coefficients. R/L_{Ti} strongly drives the turbulence destabilized by electromagnetic effects at low k_y ($k_y\rho_s \lesssim 0.2$). In this case $\gamma_{E \times B}$ has a strong stabilizing effect on the low k_y turbulence and increasing R/L_{Ti} and $\gamma_{E \times B}$ simultaneously leads to a weak variation of the transport coefficients, as observed experimentally. These results indicate that R/L_{Ti}, despite being a strong drive for the edge turbulence, can also have a strong indirect effect through $\gamma_{E \times B}$. Considering the strong relation between R/L_{Ti} and the radial electric field found experimentally and the strong effect of the isotope mass on the edge turbulence [8, 18, 19], a key role of the ion turbulent heat transport in the higher L-H power threshold at lower isotope mass is supported by these simulations. In contrast, according to our

gyro-kinetic results, increasing R/L_n to increase the edge radial electric field (and the external flow shear) to induce the L-H transition might be experimentally less effective than doing the same with R/L_{Ti}.

Finally, an effort to understand the feasibility of the development of quasi-linear models for the edge turbulence has been done comparing the linear and the non-linear results from our gyro-kinetic simulations. Differences between the properties of the turbulence in non-linear simulations and the properties of the linear instabilities have been observed, in particular when nonlinear electromagnetic effects or intermediate k_y are important for the turbulence. This represents an obstacle for the development of quasi-linear models for the edge transport, nevertheless solutions can be found and more studies should be done in this sense. As indicated in ref. [13, 14] and observed also in ref. [8], the parameter $\hat{\beta} = \beta_e \left(qR_0/L_\perp\right)^2$, where q is the safety factor and $L_\perp$ the perpendicular characteristic length, could be used as a proxy for the critical threshold above which the nonlinear electromagnetic effects play a role. Regarding the discrepancies between linear and nonlinear simulations for the intermediate k_y region, it is found that linear instabilities at finite k_x show properties similar to those in the nonlinear saturated state and might play an important role for the edge turbulence. This is supported by the fact that, differently from what is usually observed in standard core simulations, the turbulence has important contributions from the finite k_x region of the spectra.

Acknowledgement

Data Availability Statement

The data regarding the gyro-kinetic simulations that support the findings of this study are available from the corresponding author upon reasonable request. Raw data were generated at the ASDEX Upgrade and JET-ILW large scale facility. Derived data supporting the findings of this study are available from the corresponding author upon reasonable request.

References

[1] A. E. Hubbard, D. G. Whyte, R. M. Churchill, I. Cziegler, A. Dominguez, T. Golfinopoulos, J. W. Hughes, J. E. Rice, I.Bespamyatnov, M. J. Greenwald et al., Phys. Plasmas 18, 056115 (2011)

[2] P. Manz, T. Happel, U. Stroth, T. Eich, D. Silvagni, 2020 Nucl. Fusion 60 096011

[3] A. E. Hubbard, R. L. Boivin, R. S. Granetz, M. Greenwald, J. W. Hughes, I. H. Hutchinson, J. Irby, B. LaBombard, Y. Lin, E. S. Marmar et al., 2001 Phys. Plasmas 8 2033–40

[4] L. Gil, C. Silva, T. Happel, G. Birkenmeier, G.D. Conway, L. Guimarais, A. Kallenbach, T. Pütterich, J. Santos, P.A. Schneider, 2020 Nucl. Fusion 60 054003

[5] F. Ryter, T. Pütterich, M. Reich, A. Scarabosio, E. Wolfrum, R. Fischer, M. Gemisic Adamov, N. Hicks, B. Kurzan, C. Maggi et al., Nucl. Fusion 49, 062003 (2009)

[6] E. Righi, D.V. Bartlett, J.P. Christiansen, G.D. Conway, J.G. Cordey, L.-G. Eriksson, H.P.L. De Esch, G.M. Fishpool, C.W. Gowers, J.C.M. de Haas, P.J. Harbour et al., Nucl. Fusion 39, 309 (1999)

[7] C. F. Maggi, H. Weisen, J. C. Hillesheim, A. Chankin, E. Delabie, L. Horvath, F. Auriemma, I. S. Carvalho, G. Corrigan, J. Flanagan et al., Plasma Phys. Control. Fusion 60, 014045 (2018)

[8] N. Bonanomi, C. Angioni, P.C. Crandall, A. Di Siena, C.F. Maggi, P.A. Schneider, 2019 Nucl. Fusion 59 126025

[9] P.A. Schneider, A. Bustos, P. Hennequin, F. Ryter, M. Bernert, M. Cavedon, M.G. Dunne, R. Fischer, T. Görler, T. Happel et al., 2017 Nucl. Fusion 57 066003

[10] M G Dunne, L Frassinetti, M N A Beurskens, M Cavedon, S Fietz, R Fischer, L Giannone, G T A Huijsmans, B Kurzan, F Laggner et al 2017 Plasma Phys. Control. Fusion 59 025010

[11] M G Dunne, S Potzel, F Reimold, M Wischmeier, E Wolfrum, L Frassinetti, M Beurskens, P Bilkova, M Cavedon, R Fischer et al., 2017 Plasma Phys. Control. Fusion 59 014017

[12] T. Luda, C. Angioni, M.G. Dunne, E. Fable, A. Kallenbach, N. Bonanomi, P.A. Schneider, M. Siccinio, G. Tardini, 2020 Nucl. Fusion 60 036023

[13] B. D. Scott, Phys. Plasmas 12, 062314 (2005)

[14] B. D. Scott, Plasma Phys. Control. Fusion 49, S25 (2007)

C. Bourdelle, X. Garbet, R. Singh and L. Schmitz, 2012 Plasma Phys. Control. Fusion 54 115003

[16] C. Bourdelle, C.F. Maggi, L. Chôné, P. Beyer, J. Citrin, N. Fedorczak, X. Garbet, A. Loarte, F. Millitello, M. Romanelli, 2014 Nucl. Fusion 54 022001

[17] G. De Dominici, G. Fuhr, C. Bourdelle, P. Beyer, X. Garbet, Y. Sarazin, G. L. Falchetto, 2019 Nucl. Fusion 59 126019

[18] E. A. Belli, J. Candy and R. E. Waltz Phys. Rev. Lett. 125, 015001 (2020)

[19] E. A. Belli, J. Candy and R. E. Waltz Physics of Plasmas 26, 082305 (2019)

[20] K. H. Burrell, Physics of Plasmas 4, 1499 (1997)

[21] T. S. Hahm 2002 Plasma Phys. Control. Fusion 44 A87

[22] D.G. Whyte, A.E. Hubbard, J.W. Hughes, B. Lipschultz, J.E. Rice, E.S. Marmar, M. Greenwald, I. Cziegler, A. Dominguez, T. Golfinopoulos et al., Nucl. Fusion 50 (2010) 105005

[23] F. Ryter, R. Fischer, J.C. Fuchs, T. Happel, R.M. McDermott, E. Viezzer, E. Wolfrum, L. Barrera Orte, M. Bernert, A. Burckhart et al 2017 Nucl. Fusion 57 016004

[24] F. Ryter, L. Barrera Orte, B. Kurzan, R.M. McDermott, G. Tardini, E. Viezzer, M. Bernert, R. Fischer, 2014 Nucl. Fusion 54 083003

[25] M. Schmidtmayr, J.W. Hughes, F. Ryter, E. Wolfrum, N. Cao, A.J. Creely, N. Howard, A.E. Hubbard, Y. Lin, M.L. Reinke, 2018 Nucl. Fusion 58 056003

[26] U. Plank, T. Pütterich, C. Angioni, M. Cavedon, G. D. Conway, R. Fischer, T. Happel, A. Kappatou, R. M. McDermott, P. A. Schneider, G. Tardini and M. Weiland, 2020 Nucl. Fusion 60 074001.

[27] F Ryter, M Cavedon, T Happel, R M McDermott, E Viezzer, G D Conway, R Fischer, B Kurzan, T Pütterich, G Tardini, M Willensdorfer, 2016 Plasma Phys. Control. Fusion 58 014007

[28] R. Fischer, C. J. Fuchs, B. Kurzan, W. Suttrop, E. Wolfrum, 2010 Fusion Sci. Technol. 58675

[29] U.Plank, T. Puetterich, D. Brida, M. Cavedon, G. Conway, R. Dux, M. Griener, P. Hennequin, P. Cano-Megias, D. Cruz-Zabala, R. Fischer, R. M. McDermott, D. Wendler et al., in prep. for RSI

[30] L.L. Lao, H. St. John, R.D. Stambaugh, A.G. Kellman and W. Pfeiffer, 1985 Nucl. Fusion 25 1611

[31] L.L. Lao, J.R. Ferron, R.J. Groebner. W. Howl, H. St. John, E.J. Strait and T.S. Taylor, 1990 Nucl. Fusion 30 1035

[32] P. J. Mc Carthy , Physics of Plasmas 6, 3554 (1999)

[33] L M Shao, E Wolfrum, F Ryter, G Birkenmeier, F M Laggner, E Viezzer, R Fischer, M Willensdorfer, B Kurzan, T Lunt, 2016 Plasma Phys. Control. Fusion 58 025004

[34] P. Sauter, T. Pütterich, F. Ryter, E. Viezzer, E. Wolfrum, G.D. Conway, R. Fischer, B. Kurzan, R.M. McDermott, S.K. Rathgeber, 2011 Nucl. Fusion 52 012001

[35] R. M. McDermottc, B. Lipschultz, J. W. Hughes, P. J. Catto, A. E. Hubbard, I. H. Hutchinson, R. S. Granetz, M. Greenwald, B. LaBombard, K. Marr, M. L. Reinke, J. E. Rice and D. Whyte, Physics of Plasmas 16, 056103 (2009)

[36] E. Viezzer, T. Pütterich, G.D. Conway, R. Dux, T. Happel, J.C. Fuchs, R.M. McDermott, F. Ryter, B. Sieglin, W. Suttrop, M. Willensdorfer and E. Wolfrum, 2013 Nucl. Fusion 53 053005

[37] Pereverzev G. V. and Yushmanov P. N. 2002 Technical Report IPP 5/98, Max-Planck-Institut fur Plasmaphysik, Garching.

[38] E Fable, C Angioni, F J Casson, D Told,AAIvanov, F Jenko, R M McDermott, S Yu Medvedev, GVPereverzev, F Ryter, W Treutterer, E Viezzer, Plasma Phys. Control. Fusion 55, 124028 (2013)

[39] F. Jenko, W. Dorland, M. Kotschenreuther, and B. N. Rogers , Phys. Plasmas 7, 1904 (2000).

[40] T. Görler, X. Lapillonne, S.Brunner, T. Dannert, F.Jenko, F. Merz, D. Told, J. Comput. Phys. 230, 7053 (2011).

[41] E. A. Frieman and Liu Chen, Physics of Fluids 25, 502 (1982).

[42] Brizard A. J., Hahm T. S., Rev. Mod. Phys. 79, 421 (2007).

[43] J. Candy, R. E. Waltz and W. Dorland, Phys. Plasmas 11, L25 (2004)

[44] B. F. McMillan, X. Lapillonne, S. Brunner, L. Villard, S. Jolliet, A. Bottino, T. Görler, and F. Jenko, Phys. Rev. Letter 105, 155001 (2010)

[45] Y. B. Kim, P. H. Diamond, and R. J. Groebner, 1991 Phys. Fluids B 3 2050

[46] R. Singh, S. Brunner, R. Ganesh, and F. Jenko, Phys. Plasmas 21, 032115 (2014)

[47] Y. Kishimoto, J-Y. Kim, W. Horton, T. Tajima, M. J. LeBrun and H. Shirai, 1999 Plasma Phys. Control. Fusion 41 A663

[48] F. Jenko, D. Told, P. Xanthopoulos, F. Merz, and L. D. Horton, Physics of Plasmas 16, 055901 (2009)

[49] Y. Camenen, Y. Idomura, S. Jolliet and A.G. Peeters, Nucl. Fusion51(2011) 073039

[50] P. Migliano, Y. Camenen, F. J. Casson, W. A. Hornsby, and A. G. Peeters, Physics of Plasmas 20, 022101 (2013)

[51] Hua-sheng Xie and Bo Li, Physics of Plasmas 23, 082513 (2016)

[52] Z. X. Lu, X. Wang, Ph. Lauber, E. Fable, A. Bottino, W. Hornsby, T. Hayward-Schneider, F, Zonca and C. Angioni, 2019 Plasma Phys. Control. Fusion 61 044005

	$I_p(MA)$	$B_T(T)$	$\bar{n}_e(10^{19}m^{-3})$	q_{95}	Isotope	Main heating
AUG #36982	0.8	2.5	2	5	D	ECRH
AUG #37908	1.2	2.5	2	3.6	D	ECRH
AUG # 38174,38175	1.2	2.5	2	3.6	H	ECRH
AUG # 36983,36984,35842 35843,35191,35202 35204,35206,35237	0.8	2.5	$3-4$	5	D	ECRH
AUG #37909	1.2	2.5	$3-4$	3.6	D	ECRH
AUG # 35229,35241 35263,35266	0.8	2.5	$3-4$	5	H	NBI+ECRH
AUG # 38176, 38177	1.2	2.5	$3-4$	3.6	H	ECRH
JET# 89722 -> 89725	2.5	3.0	$3-4$	3	D	NBI
JET# 91433, 91434 91448 -> 91453	2.5	3.0	$3-4$	3	H	NBI

Table 1: *Main plasma parameters of the ASDEX Upgrade (AUG) and JET-ILW shots analyzed in this paper.*

Tables

T_i/T_e	ν_e^*	$\hat{\nu}_{ei}$	β_e	R/L_{Te}	R/L_{Ti}	R/L_n	$s/\hat{q}$	B_{ref}	n_e	T_e
1.38	3.1	2.8	$1.52\,10^{-4}$	56	21	34	4.6/5.7	2.46	1.6	0.143

Table 2: *Plasma parameters measured at $\rho_{tor} = 0.95$ and $t = 1.8\,s$ of ASDEX Upgrade discharge #35229. $\beta_e = \frac{8\pi n_e T_e}{B_{ref}^2}$, $\nu_e^* = \nu_{ei}\frac{4}{3\sqrt{\pi}}\frac{\hat{q}R}{\epsilon^{1.5}}\frac{1}{v_{th,e}}$, $\hat{\nu}_{ei} = \nu_{ei}\cdot\frac{\rho_a}{c_s}$, where $\hat{q}$ is the safety factor, $\epsilon = \frac{r}{R}$, $v_{th,e} = \sqrt{T_e/m_e}$ and $c_s = \sqrt{T_e/m_i}$. B_{ref} is measured in Tesla, n_e in $10^{19}m^{-3}$ and T_e in keV. Other useful quantities are: $\rho_a = 0.66\,m$ (reference length in GENE simulations), $m_e/m_i = 5.44617\,10^{-4}$ and $\rho_s^* = \rho_s/\rho_a = 7.49\,10^{-4}$ where $\rho_s = \sqrt{m_i T_e}/eB_{ref}$ and $\rho_a = \sqrt{(\Phi/\pi B_{ref})_{max}}$, Φ being the toroidal magnetic flux.*
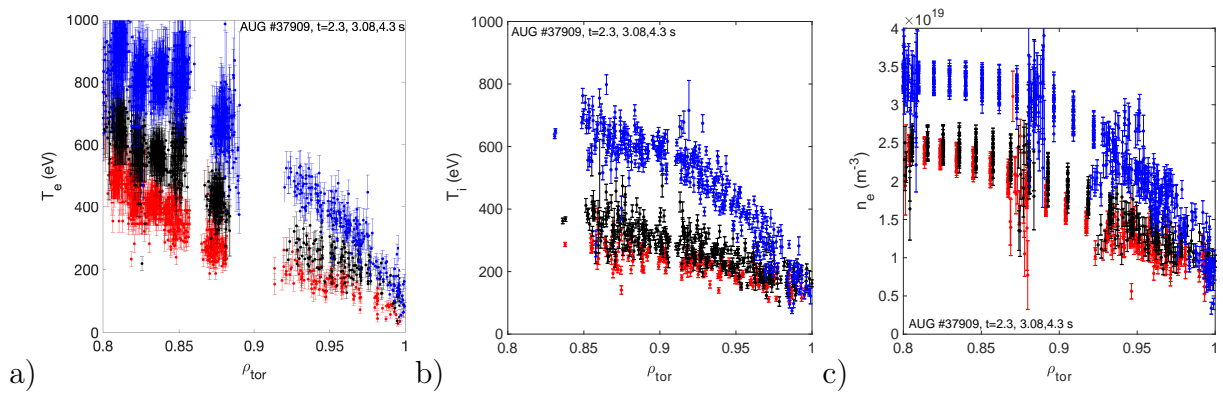
Figures

Figure 1: *Evolution of the electron temperature (a), ion temperature (b) and electron density (c) with input heating power for deuterium AUG shot #37909 at $t = 2.3\,$s (red), $t = 3.09\,$s (black) and $t = 4.3\,$s (blue). These time-steps corresponds to $P_{net}/P_{L-H} = 0.7$, 0.98, 1.5.*
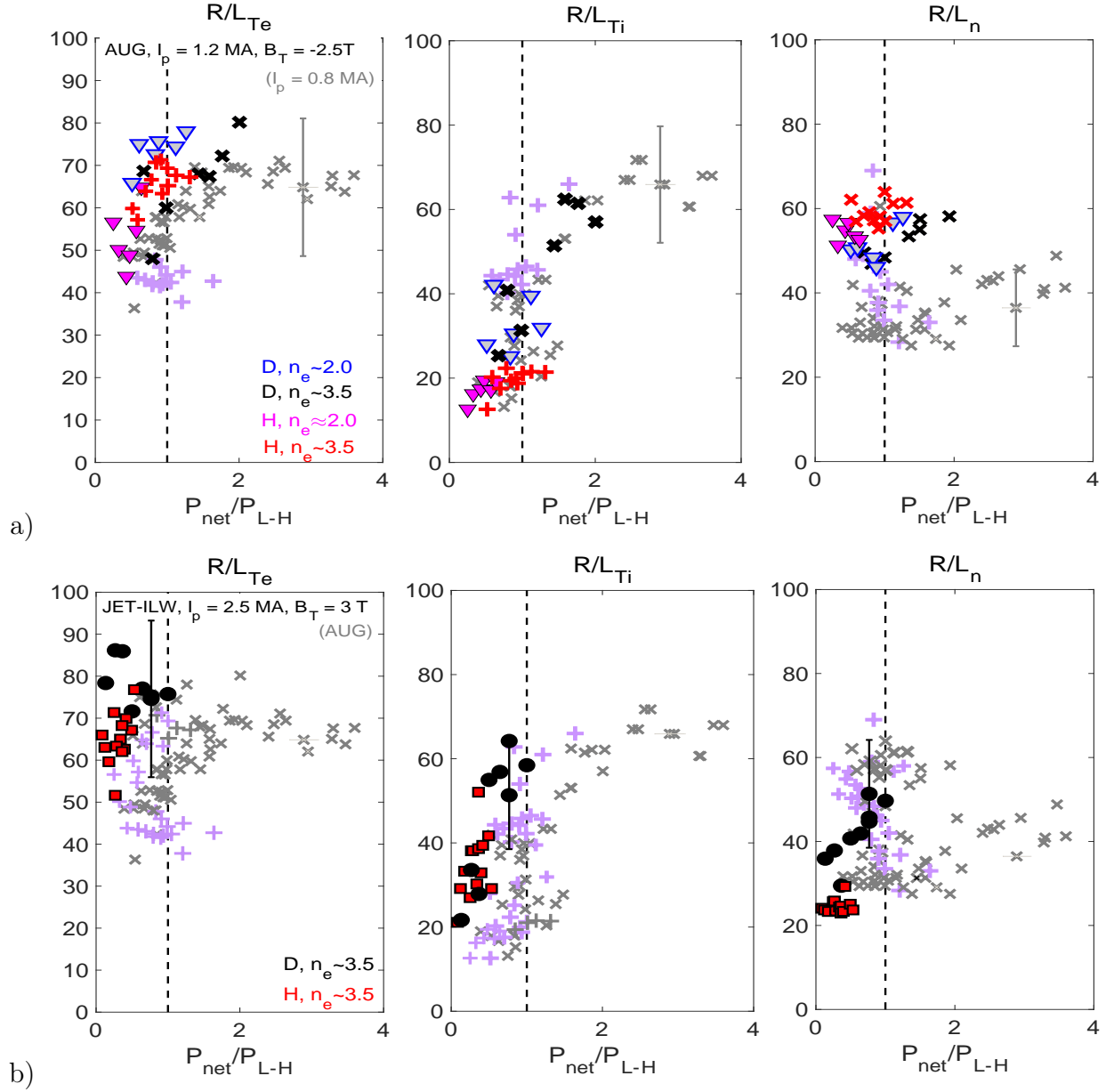
Figure 2: *Edge normalized gradients $R/L_{T_i}, R/L_{Te}, R/L_n$ evolution with P_{net}/P_{L-H} in ASDEX Upgrade (a) and JET-ILW (b). P_{net} is the net input power while P_{L-H} is the value of P_{net} at the L-H transition. In these cases P_{L-H}(hydrogen) $\sim 2P_{L-H}$(deuterium). The warm colors (red, pink, magenta) indicate values from hydrogen plasmas while cold colors (black and blue) indicate points from deuterium plasmas. The normalized gradients are calculated at $\rho_{tor} = 0.95$ from the fits of the experimental data.*
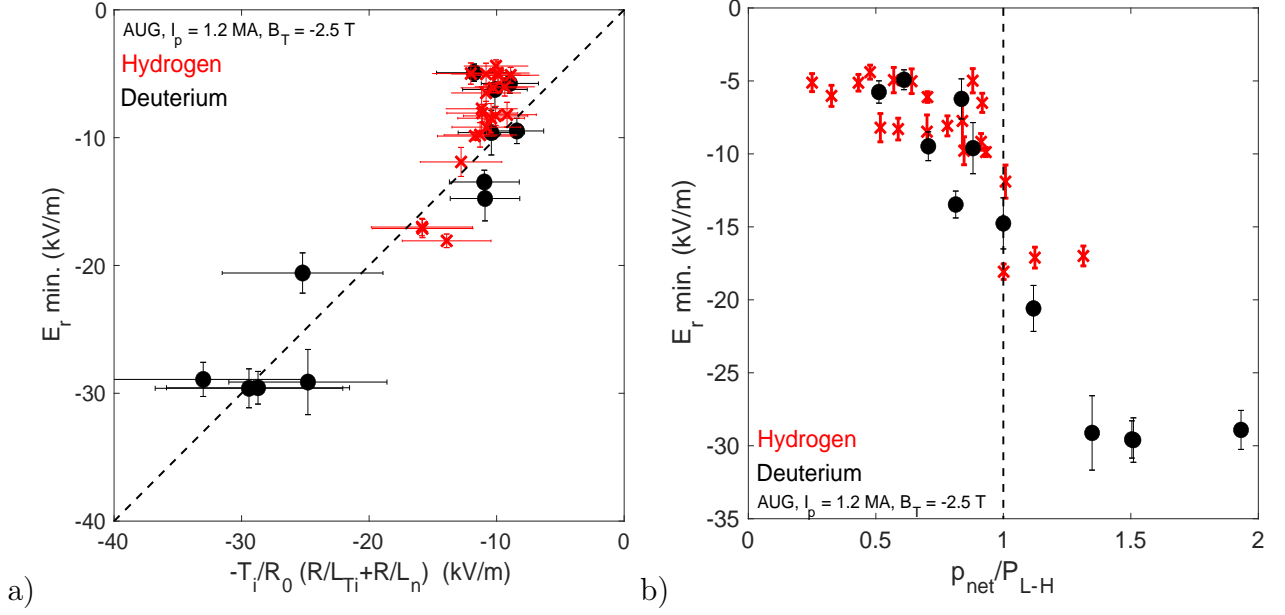
Figure 3: a) Evolution of the minimum of the edge radial electric field E_r, measured using the active helium spectroscopy signal [29], with P_{net}/P_{L-H} in the ASDEX Upgrade shots with $I_p = 1.2$ MA. b) Minimum of the edge radial electric field E_r plotted as a function of the ion diamagnetic term from the ion radial force balance equation $T_i/(q_i R_0)\,(R/L_{Ti} + R/L_n)$ measured at $\rho_{tor} = 0.95$.
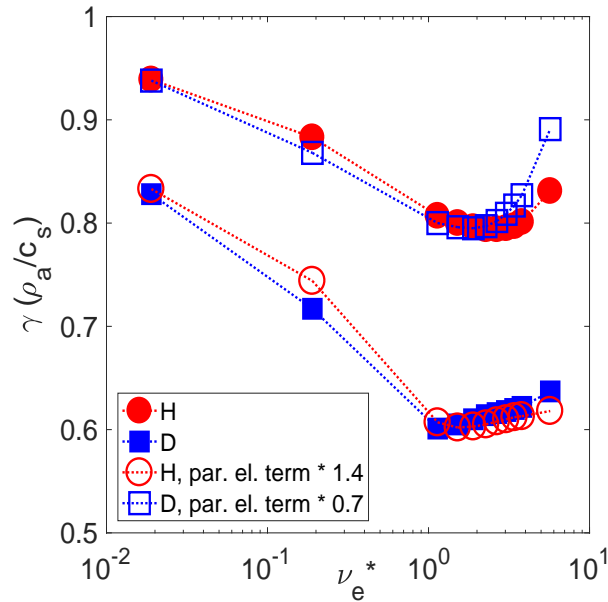
Figure 4: Linear growth rate as a function of ν_e^* from GENE linear simulations. Hydrogen simulations were repeated modifying the parallel electron dynamics term, that depends on m_e/m_i, in order to have values of m_e/m_i in this term as in deuterium simulations and vice versa. As visible this term is responsible for the effect of the main ion mass in the plasma edge conditions.
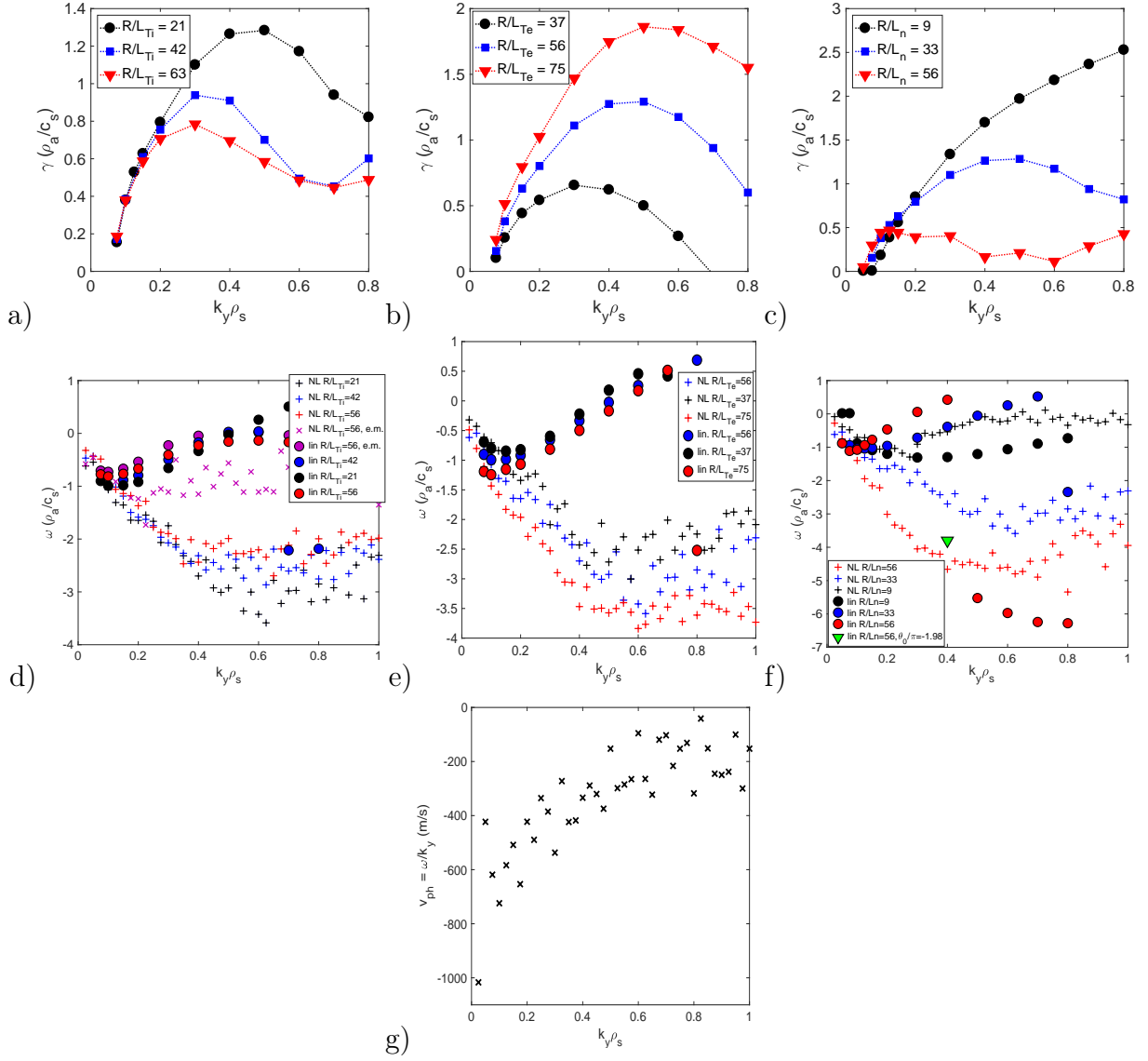
Figure 5: *Linear growth rate as a function of $k_y\rho_s$ at different values of R/L_n (c), R/L_{Te} (b) and R/L_{Ti} (a) and frequencies of the dominant instabilities and dominant frequencies of the turbulence from non-linear simulations as a function of $k_y\rho_s$ at the different values of R/L_n (f), R/L_{Te} (e) and R/L_{Ti} (d). The nominal values are $(R/L_{Ti}, R/L_{Te}, R/L_n) = (21, 33, 56)$, two of these values are kept fixed while scanning in the third one. g)Typical phase velocity of the turbulence calculated as $v_{ph} = \omega/k_y$ (m/s) for the electrostatic case with $(R/L_{Te}, R/L_{Ti}, R/L_n) = (56, 42, 33)$.*
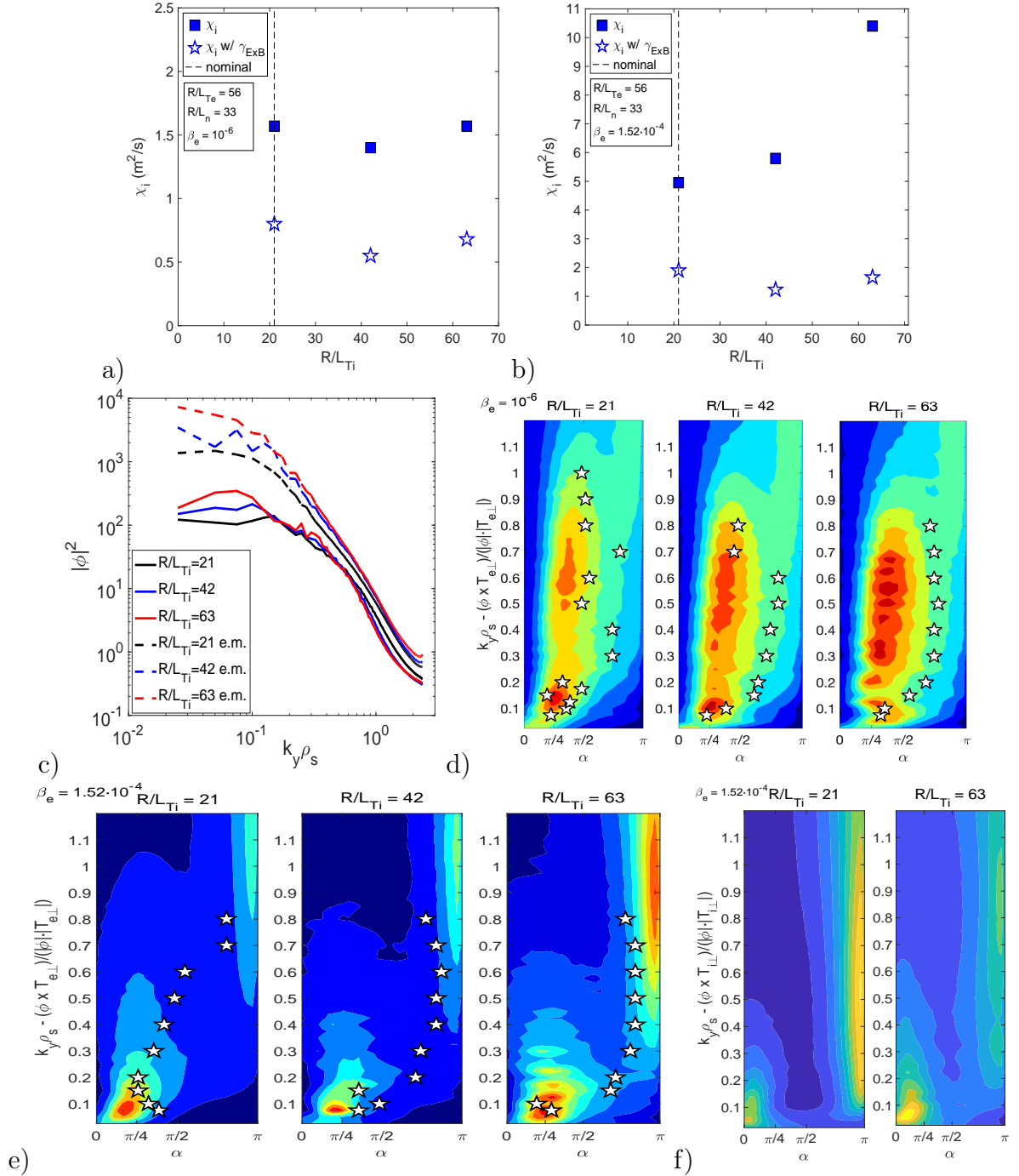
Figure 6: *a-b) Evolution of the ion heat transport coefficient $\chi_i(m^2/s)$ with R/L_{Ti} from electrostatic $(\beta_e = 10^{-6})$ and electromagnetic $(\beta_e = 1.52\,10^{-4})$ nonlinear local gyro-kinetic simulations. c) $k_y\rho_s$ spectra of $|\phi|^2$, ϕ being the perturbed electrostatic potential, from the same simulations. d-e) Normalized intensity of the cross-phases between the electrostatic potential and the perpendicular electron temperature fluctuations, $(\phi \times T_{e,\perp})/(|\phi||T_{e\perp}|)$, at different $k_y\rho_s$ as a function of the cross-phase angle α from the electrostatic and the electromagnetic simulations. The white stars represent the main values from linear simulations centered at $k_x = 0$. A zoom in the range $0.025 \leq k_y\rho_s \leq 1.2$ is applied. f) Normalized intensity of the cross-phases between the electrostatic potential and the perpendicular ion temperature fluctuations, $(\phi \times T_{i,\perp})/(|\phi||T_{i\perp}|)$, at different $k_y\rho_s$ as a function of the cross-phase angle α from the electrostatic and the electromagnetic simulations.*
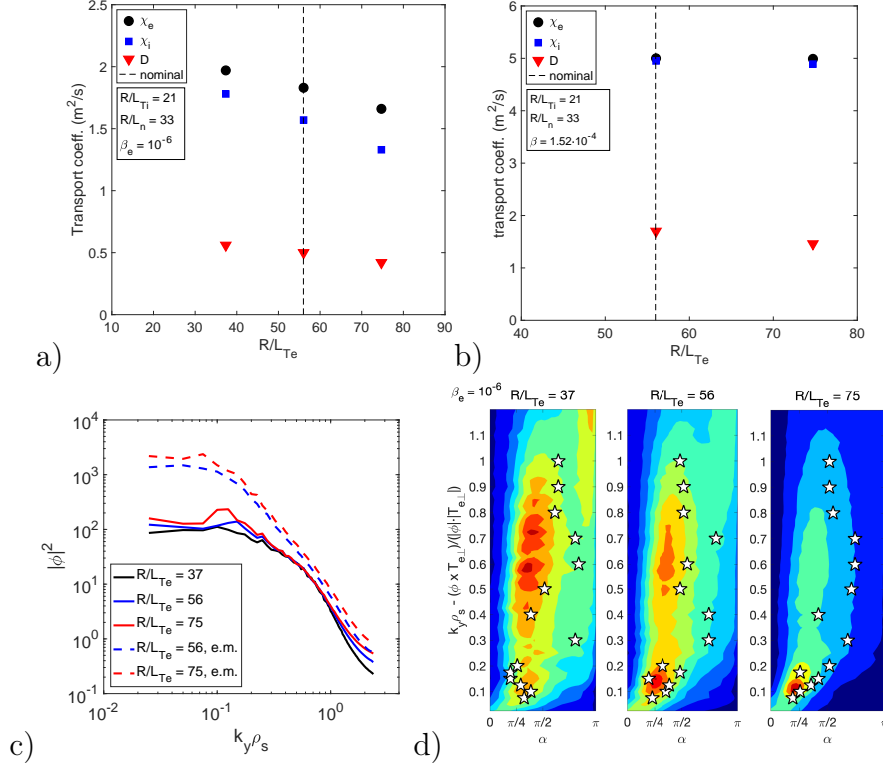
Figure 7: *a-b) Evolution of the ion and electron heat transport coefficient $\chi_{i,e}$(m²/s) and of the particle transport coefficient D (m²/s) with R/L_{Te} from electrostatic ($\beta_e = 10^{-6}$) and electromagnetic ($\beta_e = 1.52\,10^{-4}$) nonlinear local gyro-kinetic simulations. c) $k_y\rho_s$ spectra of $|\phi|^2$, ϕ being the perturbed electrostatic potential, from the same simulations. d) Normalized intensity of the cross-phases between the electrostatic potential and the perpendicular electron temperature fluctuations, $(\phi \times T_{e,\perp})/(|\phi||T_{e\perp}|)$, at different $k_y\rho_s$ as a function of the cross-phase angle α. The white stars represent the main values from linear simulations centered at $k_x = 0$. A zoom in the range $0.025 \leq k_y\rho_s \leq 1.2$ is applied.*
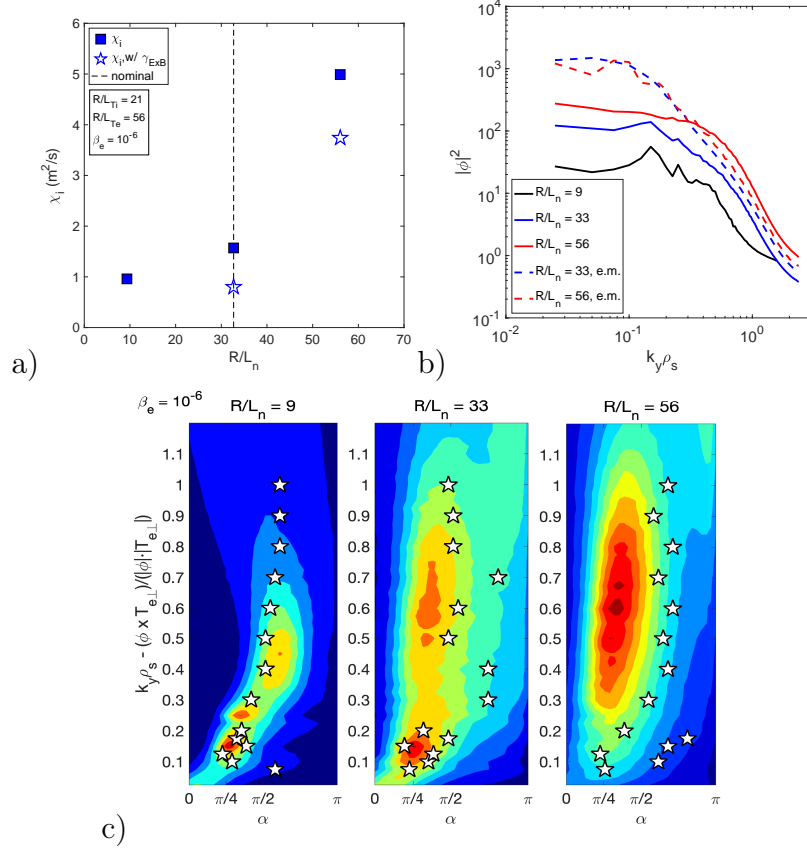
Figure 8: a) Evolution of the ion heat transport coefficient $\chi_i (\mathrm{m}^2/\mathrm{s})$ with R/L_n from electrostatic ($\beta_e = 10^{-6}$) nonlinear local gyro-kinetic simulations. b) $k_y\rho_s$ spectra of $|\phi|^2$, ϕ being the perturbed electrostatic potential, from both from electrostatic ($\beta_e = 10^{-6}$) and electromagnetic ($\beta_e = 1.52\,10^{-4}$) simulations. c) Normalized intensity of the cross-phases between the electrostatic potential and the perpendicular electron temperature fluctuations, $(\phi \times T_{e,\perp})/(|\phi||T_{e\perp}|)$, at different $k_y\rho_s$ as a function of the cross-phase angle α. The white stars represent the main values from linear simulations centered at $k_x = 0$. A zoom in the range $0.025 \le k_y\rho_s \le 1.2$ is applied.
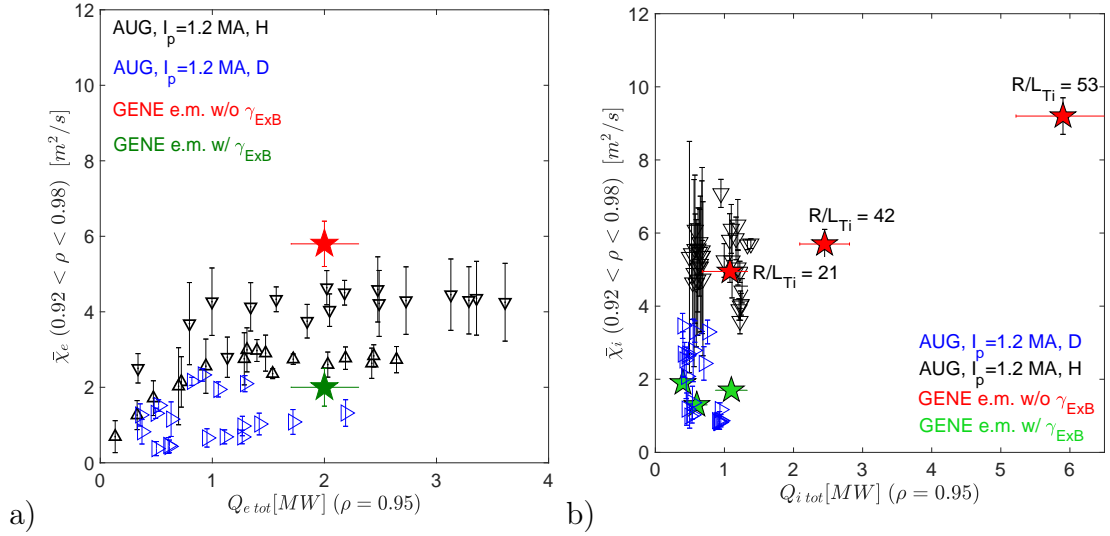
Figure 9: *Comparison between the experimental values of the electron (a) and ion (b) heat transport coefficient $\chi_{e,i}(\mathrm{m^2/s})$ and the values obtained from the nonlinear gyro-kinetic simulation. The experimental values were evaluated using ASTRA power balance calculations of the ASDEX Upgrade discharges in hydrogen and averaging inside $0.92 < \rho_{tor} < 0.98$. Blue points indicate discharges with $I_p = 0.8\,\mathrm{MA}$ while black points indicate discharges with $I_p = 1.2\,\mathrm{MA}$. The red stars indicate the values from GENE simulation without $\hat{\gamma}_{ExB}$ while green stars indicate the values from GENE simulations where the effect of $\hat{\gamma}_{ExB}$ was taken into account. These quantities are plotted as a function of the electron and ion heat fluxes in MW and measured at $\rho_{tor} = 0.95$. No visible evolution of the transport coefficient with input power is visible experimentally. When taking into account the external flow shear the experimental values and trends are in good comparison with the values from the simulations, even if in these cases we did not try to match the experimental values by varying parameters such as β_e.*
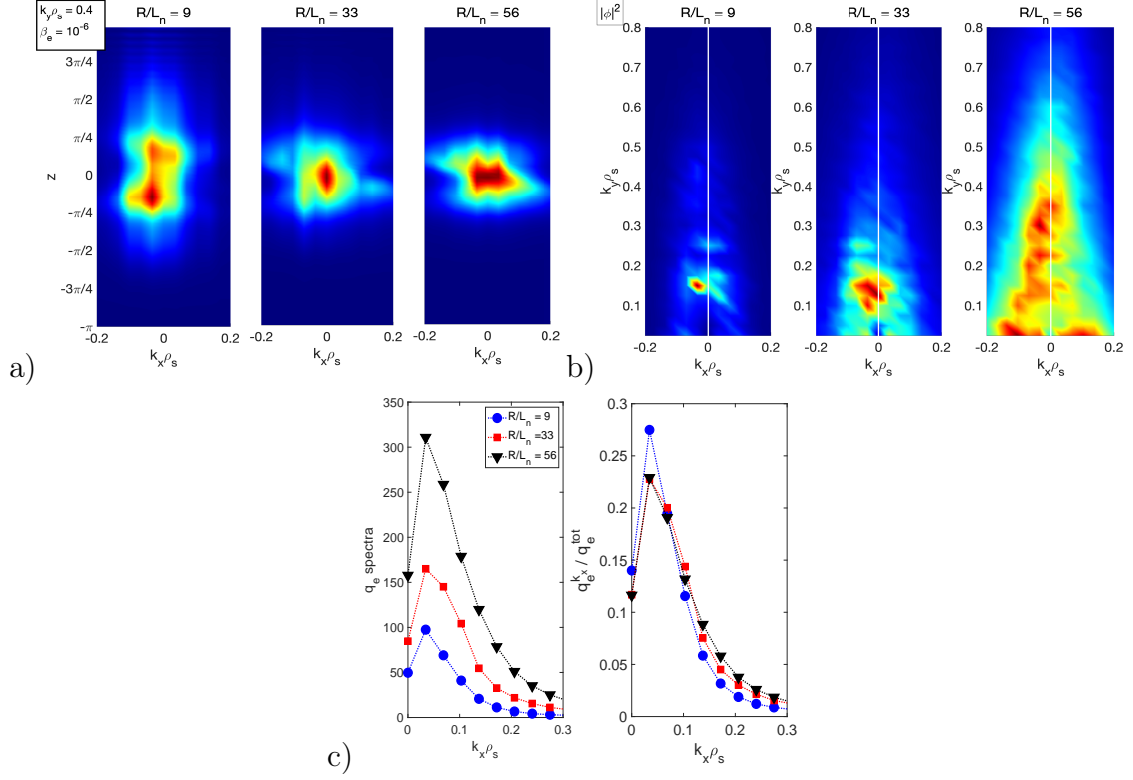
Figure 10: *a-b) $|\phi|^2$ plotted in $(k_x\rho_s, z)$ and in $(k_x\rho_s, k_y\rho_s)$ space from electrostatic GENE simulations at different values of R/L_n. The values are averaged over the other dimensions. c) Electron heat flux (integrated over k_y and z) k_x spectra at different values of R/L_n from the same simulations of figures a) and b). The ratio between the contribution to the total heat flux from each value of $k_x\rho_s$ and the total heat flux, $q_e^{k_x}/q_e^{tot}$, is also reported.*
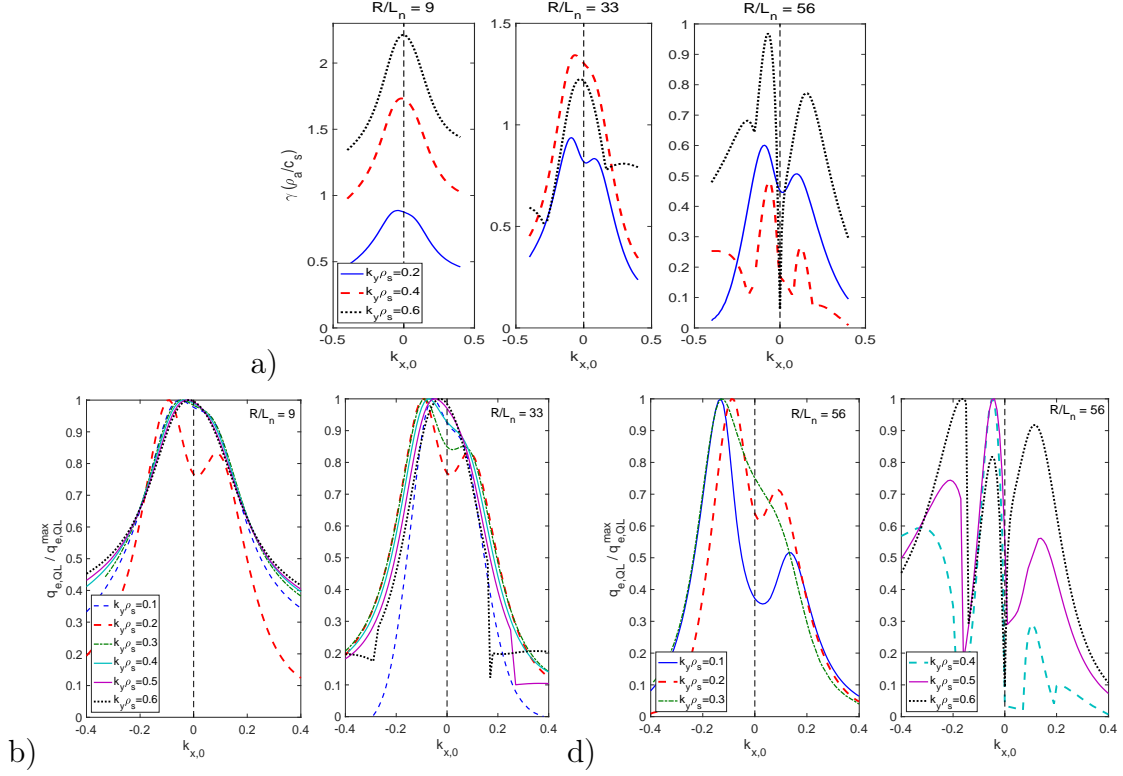
31

Figure 11: *a) Linear growth rate of the main linear instabilities as a function of $k_{x,0}$ for different values of $k_y\rho_s$ and R/L_n. b-c) Quasi-linear electron heat flux as a function of $k_{x,0}$ computed at different values of $k_y\rho_s$ and R/L_n. Both γ and q_e^{QL} show peaks at finite value of $k_{x,0}$. The quasi-linear electron heat flux is computed as $q_e^{QL} = \sum_{k_y} \frac{\gamma_{k_y}}{\langle k_\perp^2 \rangle} \frac{q_e^{k_y}}{|\phi_{k_y}|^2}$, where $\langle k_\perp^2 \rangle = \int (g_{yy}k_y^2 + 2g_{xy}k_xk_y + g_{xx}k_x^2) \, |\phi|^2 J dk_x dz / \int |\phi|^2 J dk_x dz$, $q_e^{k_y}$ and γ_{k_y} are the electron heat flux and the linear growth rate from linear simulations at fixed k_y and J, g_{ij} are related to the geometry of the flux surface.*
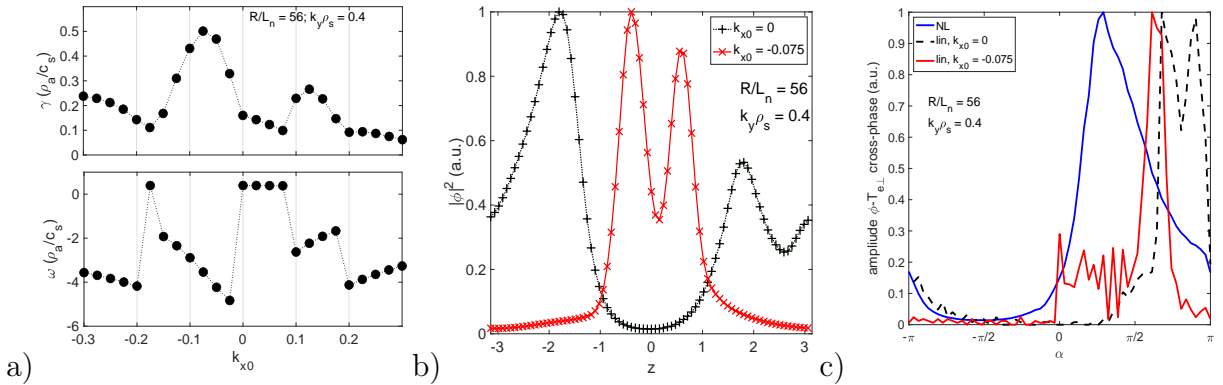

Figure 12: *a) Growth rate and frequency of the dominant instability from linear simulations at $k_y\rho_s = 0.4$ and using $R/L_n = 56$ as a function of the central value of k_x. The growth rate peaks for instabilities centered at $k_x = -0.075$ with a negative value of the frequency. b) Electrostatic potential parallel (z) structures for the instability centered at $k_x = 0$ (black) and at $k_x = -0.075$ (red). c) $\phi - T_{e\perp}$ cross-phases values from non-linear simulations (blue), for the linear instability centered at $k_x = 0$ (black) and for the linear instability centered at $k_x = -0.075$ (red).*
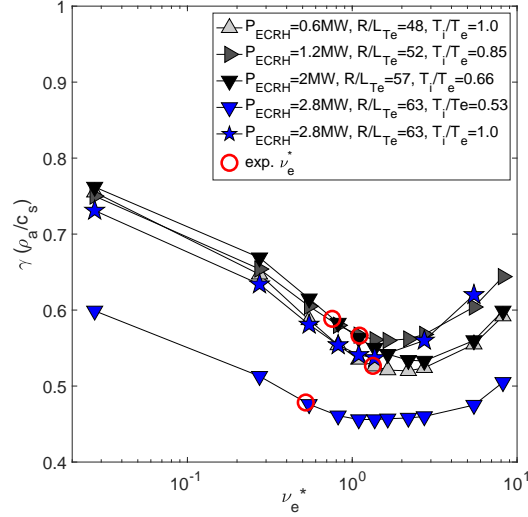
Figure 13: *Linear scan made using input parameters taken from AUG shots #36982 in deuterium (see Table1) at different levels of ECRH power and changing all the parameters consistently. The scan was made using $k_y\rho_s = 0.2$, where the nonlinear fluxes usually peak in edge simulations, and scanning in collisionality to see where the minimum in $\gamma(\nu_e^*)$ is located with respect the experimental values of ν_e^*. Despite the increasing R/L_{Te} with increasing ECRH power, the linear growth rates are lower close to the L-H transition ($P_{ECRH} = 2.8\,\mathrm{MW}$). In this case T_e/T_i is found to be an important parameter.*